Journal of Optics

PAPER

Complex spatial coherence measurement using phase-shifting wavefront-inversion interferometry

To cite this article: Pranay Mohta *et al* 2025 *J. Opt.* **27** 075606

IOP Publishing Journal of Optics
J. Opt. 27 (2025) 075606 (12pp) https://doi.org/10.1088/2040-8986/adec00

Complex spatial coherence measurement using phase-shifting wavefront-inversion interferometry

Pranay Mohta[1], Abhinandan Bhattacharjee[2] and Anand K Jha[1,*]

[1] Department of Physics, Indian Institute of Technology Kanpur, Kanpur, UP 208016, India
[2] Universität Paderborn, Warburger Strasse 100, 33098 Paderborn, Germany

E-mail: akjha@iitk.ac.in, mohtapranay01@gmail.com and arko.hkd@gmail.com

Received 7 March 2025, revised 28 June 2025
Accepted for publication 4 July 2025
Published 24 July 2025

Abstract

Accurate measurement of the spatial coherence function is critical for applications ranging from imaging to communication. However, accurate measurement of arbitrary complex spatial coherence function still remains a significant challenge. In this work, we present a phase-shifting wavefront-inversion and shearing interferometric technique which enables direct, noise-insensitive measurement of the complex cross-spectral density function for a very broad class of fields, which includes all spatially stationary fields and the physically most relevant class of spatially non-stationary fields. By integrating the phase-shifting technique with wavefront inversion interferometry, we implement an intensity difference protocol that eliminates all phase-insensitive noise, significantly enhancing measurement fidelity. Experimental results validate the method's robustness and accuracy, demonstrating its applicability to both stationary and non-stationary fields, and extending its utility to single-photon-level measurements. This technique represents a promising tool for all coherence-driven applications.

Keywords: interferometry, spatial coherence, spatial coherence measurement, partial coherence

1. Introduction

Characterizing the spatial coherence of optical fields is a fundamental pursuit in optics, with implications ranging from imaging to communication. The spatial coherence, quantified by the cross-spectral density function, is a key descriptor of correlation between the electric field at two spatial locations in an optical field. In the quantum picture, it corresponds to the density matrix elements in the position basis. Spatially partially coherent fields find various applications such as optical coherence tomography (OCT) [1], imaging through turbulence [2, 3], coherence holography [4], photon correlation holography [5], optical communication [6], and particle trapping [7].

While many spatially partially coherent light sources utilized in practical applications are spatially stationary, the spatially non-stationary sources are often encountered in real-world situations and are equally important for applications. For instance, the simplest optical system, a thin lens, introduces a quadratic phase in an optical field passing through it and is thus spatially non-stationary. The coherence function for free space propagation of a spatially incoherent source is of quadratic nature (see section 5.7 of [8]). In non-line-of-sight imaging, the coherence function exhibits a quadratic nature, holding crucial information about the object's distance from the detector [9]. Recent research has seen a surge of interest in non-uniform coherence function, specifically those dependent on the difference of square of spatial coordinates, due to their unique propagation characteristics. These beams find applications in coherence-based optical encryption [10], simultaneous optical trapping of two types of Rayleigh particles with

* Author to whom any correspondence should be addressed.

different refractive indices [11], and the generation of self-focusing [12] and multi-focusing beams [13].

Young's double-slit interferometer [14] is the classic technique for measuring the spatial coherence function. Despite advancements in its implementation, this method and its variants [15, 16] suffer from drawbacks such as low light efficiency, long measurement times, and stability requirements. To address these limitations, alternative methods have been introduced, including shearing interferometers [17], Sagnac interferometers [18], phase-space tomography [19], and techniques based on shadows [20], gratings [21], masks [22], obstacles [23], and fiber optics [24]. However, these methods often work well only for the coherence function of a specific form or reliably measure only its amplitude. Other explored methods include, the free-space propagation methods [25, 26] and generalized Hanbury Brown–Twiss method [27]. The free-space propagation methods require prior knowledge of the coherence properties, and their iterative phase retrieval can fail to converge correctly. The generalized Hanbury Brown–Twiss method can measure the complex coherence function but needs a pair of coherent reference fields. Despite these advancements, the wavefront-inversion interferometer remains one of the most important tools for coherence characterization. Its conventional implementation [28, 29], however, has significant limitations. Primarily, it can only measure the amplitude of the coherence function, missing crucial phase information. Additionally, due to the finite edge width of the prism used, the scheme [28] misses out on some information. Recent advancements have sought to address these issues. Accurate coherence function measurement was demonstrated in [30] but was limited to real and spatially stationary coherence functions. Reference [31] extended this to arbitrary coherence functions, but the Fourier transform method used is highly sensitive to noise, which can distort phase and amplitude extraction and the edge effects due to non-periodic fringe patterns lead to spectral leakage. As discussed in [32], while windowing techniques like the Hanning window can mitigate these edge artifacts, they degrade resolution and reduce the effective analysis area. The method also cannot be easily extended to broadband fields, as the interfering wavefronts are tilted with respect to one another, requiring path-length compensation for each measurement point. Additionally, the placement of mirrors outside the interferometer's plane for wavefront rotation, reduces the mechanical stability of the interferometer in [31] and makes it less compact. Reference [33] addressed compactness by using two lenses for wavefront inversion but retained the limitations of the Fourier method in [31].

In summary, while accurate techniques exist for measuring real-valued spatially stationary coherence functions, no current method can accurately measure the complex spatial coherence function of both stationary and non-stationary fields in a reference-free and noise-insensitive manner. In contrast, in this article, we report experimental demonstration of an accurate, noise-insensitive and reference-free technique for directly measuring the complex cross-spectral density functions of a broad class of cross-spectral density functions, which depend either on the difference of spatial coordinates, or squares of spatial coordinates, or both. This class of fields include all spatially stationary fields and the physically most relevant class of spatially non-stationary fields. Furthermore, if the optical field is temporally stationary, our technique also works with broadband fields.

2. Theory

Figure 1(d) shows the schematic diagram of our proposed experimental technique, which involves a modified Mach–Zehnder type interferometer. The cross-spectral density function of the field at two space points $\boldsymbol{\rho_1}$ and $\boldsymbol{\rho_2}$, is defined as $W(\boldsymbol{\rho_1},\boldsymbol{\rho_2}) = \langle E^*_{\rm in}(\boldsymbol{\rho_1})E_{\rm in}(\boldsymbol{\rho_2})\rangle$, where $\langle\cdots\rangle$ denotes ensemble average over various realizations of the field, and $E_{\rm in}(\boldsymbol{\rho_1})$, and $E_{\rm in}(\boldsymbol{\rho_2})$ are the electric fields at the two spatial locations. One of the dove prisms inverts the incoming wavefront about the x-axis and the other one about the y-axis. Dove prisms ensure mechanical stability and keeps the interferometer compact but it can introduce corner obstructions and front surface reflections. To mitigate these drawbacks, an image rotator, constructed as described in [34], can be used in its place. As we work with linearly polarized light, the chosen configurations of the dove prisms does not alter the polarization state [34]. Arm-1 of the interferometer contains a geometric phase unit comprising two quarter-wave plates oriented at 45° with respect to the polarization of light and a half-wave plate (HWP) in between. Rotating the HWP by an angle θ introduces a geometric phase of 2θ [35]. Translating the source in the x-direction by x_0, we introduce a shear of $2x_0$ between the two interfering wavefronts. Figure 1(e) illustrates the resulting wavefronts at the output port of the interferometer, which can be expressed as

$$E_{\rm out}(\boldsymbol{\rho}) \equiv E_{\rm out}(x,y) = k_1E_{\rm in}(-x+x_0,y)\,\mathrm{e}^{\mathrm{i}(\omega_0 t_1+\beta_1)} + k_2E_{\rm in}(x+x_0,-y)\,\mathrm{e}^{\mathrm{i}(\omega_0 t_2+\beta_2)} \quad (1)$$

where the time taken by the field to travel through the two arms is t_1 and t_2; ω_0 is the central frequency of the field; β_1 and β_2 are phases other than the dynamical phase acquired by the field; and k_1 and k_2 are the arm constants. We assume that t_2-t_1 is less than the coherence time of the field. The intensity $I_{\rm out}(x,y) \equiv \langle E^*_{\rm out}(x,y)E_{\rm out}(x,y)\rangle$ at the output of the interferometer is given by

$$\begin{aligned} I_{\rm out}(x,y) = {} & |k_1|^2 I_1(-x+x_0,y) + |k_2|^2 I_2(x+x_0,-y) \\ & + 2k_1k_2\mathrm{Re}\left[W(-x+x_0,y;x+x_0,-y)\right]\cos\delta \\ & - 2k_1k_2\mathrm{Im}\left[W(-x+x_0,y;x+x_0,-y)\right]\sin\delta \\ & + I_{\rm b}(x,y), \end{aligned} \quad (2)$$

where $\delta = \omega_0(t_2-t_1)+(\beta_2-\beta_1)$. We express $\langle E^*_{\rm in}(-x+x_0,y)E_{\rm in}(-x+x_0,y)\rangle = I_1(-x+x_0,y)$, $\langle E^*_{\rm in}(x+x_0,-y)E_{\rm in}(x+x_0,-y)\rangle = I_2(x+x_0,-y)$ and $W(-x+x_0,y;x+x_0,-y) = \langle E^*_{\rm in}(-x+x_0,y)E_{\rm in}(x+x_0,-y)\rangle$. Re$[\cdots]$ and Im$[\cdots]$ denote the real and imaginary parts. The contribution $I^{\delta}_{\rm b}(x,y)$ is

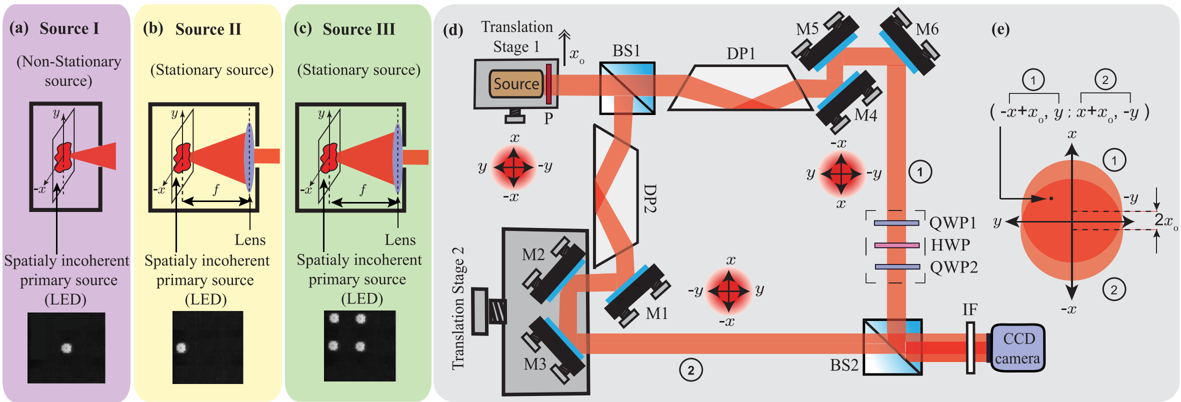

Figure 1. (a)–(c) are the three light sources used. (d) Schematic diagram of the experimental setup. There is one dove prism in each arm, at 90° to one another, and one arm contains a geometric phase module which consists of two quarter waveplates at 45° and a half waveplate in between. The length of each interferometric arm is about 41 cm, and the CCD camera is kept at about 7 cm from the beam splitter (BS2). An interference filter (IF) centered at 632 nm having a wavelength bandwidth of 10 nm is used before the CCD camera. (e) The two interfering wavefronts at the CCD camera plane. The wavefront coming through one interferometric arm is inverted in the y direction and the wavefront coming through the other arm is inverted in the x direction with respect to the input wavefront. BS stands for beam splitter, M for mirror, IF for interference filter, QWP for quarter waveplate, HWP for half waveplate and DP for dove prism, x_0 is the shear in x-direction.

the background noise. If $I_{\text{out}}^{\delta_c}(x,y)$ and $I_{\text{out}}^{\delta_d}(x,y)$ are the output intensities measured at $\delta=\delta_c$ and $\delta=\delta_d$, the difference intensity is

$$\begin{aligned}\Delta I_{\text{out}}^{(\delta_c,\delta_d)}(x,y) &= I_{\text{out}}^{\delta_c}(x,y) - I_{\text{out}}^{\delta_d}(x,y)\\ &= I_{\text{b}}^{\delta_c}(x,y) - I_{\text{b}}^{\delta_d}(x,y)\\ &\quad + 2k_1k_2\{\text{Re}[W(-x+x_0,y;x+x_0,-y)]\\ &\quad \times(\cos\delta_c-\cos\delta_d)\\ &\quad -\text{Im}[W(-x+x_0,y;x+x_0,-y)]\\ &\quad \times(\sin\delta_c-\sin\delta_d)\}. \end{aligned} \tag{3}$$

Since the background noise does not depend on δ, we get $I_{\text{b}}^{\delta_c}(x,y)-I_{\text{b}}^{\delta_d}(x,y)\approx 0$. Therefore, setting $\delta_c=0$ and $\delta_d=\pi$, we get

$$\text{Re}[W(-x+x_0,y;x+x_0,-y)] = \Delta I_{\text{out}}^{(0,\pi)}(x,y)/4k_1k_2 \tag{4}$$

and setting $\delta_c=3\pi/2$ and $\delta_d=\pi/2$, we get

$$\text{Im}[W(-x+x_0,y;x+x_0,-y)] = \Delta I_{\text{out}}^{(3\pi/2,\pi/2)}(x,y)/4k_1k_2. \tag{5}$$

Thus, by measuring the difference intensities $\Delta I_{\text{out}}^{(0,\pi)}(x,y)$ and $\Delta I_{\text{out}}^{(3\pi/2,\pi/2)}(x,y)$, we obtain the real and imaginary parts to within the same scaling factor $4k_1k_2$. This way, we obtain the complex cross-spectral density function $W(-x+x_0,y;x+x_0,-y)$ in a four-shot manner, which not only obviates the necessity for the precise knowledge of k_1, k_2, I_1 and I_2 but also becomes completely insensitive to background noise figure 3.

Knowing the real and imaginary parts, one can find the amplitude and phase as:

$$|W(-x+x_0,y;x+x_0,-y)|^2 = \frac{\left(\Delta I_{\text{out}}^{(0,\pi)}\right)^2+\left(\Delta I_{\text{out}}^{(3\pi/2,\pi/2)}\right)^2}{4k_1k_2} \tag{6}$$

$$\arg[W(-x+x_0,y;x+x_0,-y)] = \tan^{-1}\left[\frac{\Delta I_{\text{out}}^{(3\pi/2,\pi/2)}}{\Delta I_{\text{out}}^{(0,\pi)}}\right]. \tag{7}$$

The amplitude of the cross-spectral density function determines the visibility of interference fringes and, when the two spatial locations are the same, reduces to the spectral density (i.e. the local intensity). The phase represents the relative phase difference between the fields at two points, governing whether the interference is constructive or destructive, and also encodes information about the wavefront shape and propagation characteristics.

Our aim is to measure a class of spatially non-stationary field for which the complex cross-spectral density function factorizes as $W(x_1,x_2;y_1,y_2)=W_x(x_1,x_2)W_y(y_1,y_2)$, with the cross-spectral density in x- and y-directions being of the form $W(x_1,x_2)=W_1(x_2-x_1)W_2(x_2^2-x_1^2)$. This is the most commonly-encountered class of fields [9–13]. It becomes spatially stationary in situations in which $W_2(x_2^2-x_1^2)=1$. In what follows, for conceptual clarity, we only consider the x-coordinate, noting that the same principles can be extended to the y-coordinate. Setting $x_2=x+x_0$ and $x_1=-x+x_0$ with the shear $x_0=0$ and thus taking $W_2(0)=1$, we obtain

$$W(-x,x)=W_1(2x)W_2(0)=W_1(2x)=A_1(2x)\,\text{e}^{\text{i}\phi_1(2x)}. \tag{8}$$

By employing the above four-shot technique, one can measure $W(-x,x)=W_1(2x)$ and thereby the amplitude $A_1(2x)$ and phase $\phi_1(2x)$. The phase $\phi_1(2x)$, which is indeterminate up to

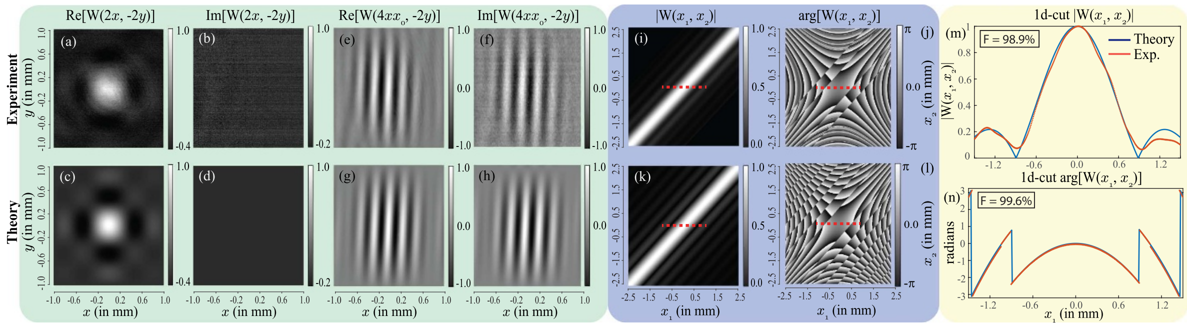

Figure 2. Source I: (a) and (b) The experimentally measured $\mathrm{Re}[W(-x+x_0,y;x+x_0,-y)]$ and $\mathrm{Im}[W(-x+x_0,y;x+x_0,-y)]$ (c) and (d) The theoretical $\mathrm{Re}[W(-x+x_0,y;x+x_0,-y)]$ and $\mathrm{Im}[W(-x+x_0,y;x+x_0,-y)]$ with no shear, i.e. $x_0=0$ and $y_0=0$. (e)–(h) Is the same with shear $x_0=2.5$ mm and $y_0=0$ mm. (i) and (j) The experimentally reconstructed $|W(x_1,x_2)|$ and $\arg[W(x_1,x_2)]$. (k) and (l) The theoretical $|W(x_1,x_2)|$ and $\arg[W(x_1,x_2)]$. (m) and (n) The 1d-cut of $|W(x_1,x_2)|$ and $\arg[W(x_1,x_2)]$ along the dotted red line.

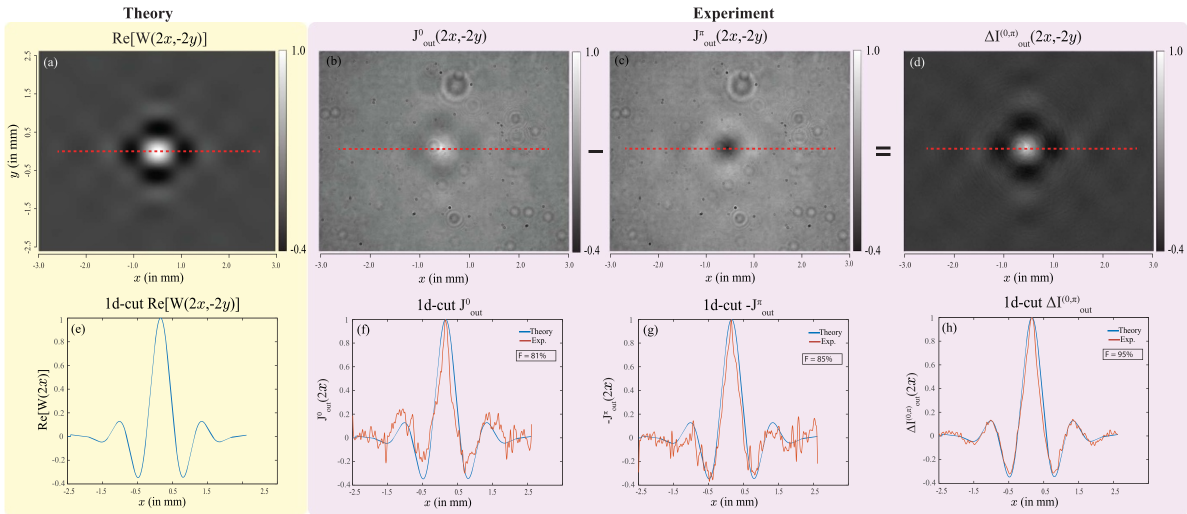

Figure 3. Illustrates how subtracting the intensities effectively removes phase-insensitive background noise, enabling accurate measurement of the cross-spectral density function. (a) The theoretical Re[W(x,y)]. (b)–(c) $J^0_{\mathrm{out}}(x,y)$ and $J^\pi_{\mathrm{out}}(x,y)$ The individual interferograms with the individual intensities from the two arms subtracted, $J^\delta_{\mathrm{out}}(x,y)=I^\delta_{\mathrm{out}}(x,y)-I_1(x,y)-I_2(x,y)$, (d) The difference intensity $\Delta I^{(0,\pi)}_{\mathrm{out}}(x,y)$. (e)–(h) The normalized 1d-cuts of the respective 2d functions along the dotted red line.

2π, is unwrapped following the algorithm described in [32] and we obtain the phase ϕ_1^u, which ranges from $-\infty$ to ∞. The function $W_1(x_2-x_1)$ is reconstructed by mapping $W_1(2x)$ to $W_1(x_2-x_1)$ with $x=(x_2-x_1)/2$. Next, setting $x_2=x+x_0$ and $x_1=-x+x_0$, with $x_0\neq 0$, we obtain

$$\begin{aligned} W(-x+x_0,x+x_0) &= W_1(2x)\,W_2(4xx_0) \\ &= A_1(2x)A_2(4xx_0)\,\mathrm{e}^{\mathrm{i}[\phi_1(2x)+\phi_2(4xx_0)]}. \end{aligned} \tag{9}$$

Again, by employing the above four-shot technique, one can measure $W(-x+x_0,x+x_0)$ and thereby the amplitude $A_2(4xx_0)$ as

$$A_2(4xx_0)=|W(-x+x_0,x+x_0)|/|W(-x,x)|. \tag{10}$$

We note that to deal with the small values of $|W(-x,x)|$ in the denominator, we set an appropriate threshold or floor value below which all the values are set to the floor value. We define ϕ^u as the unwrapped version of $\phi_1(2x)+\phi_2(4xx_0)$. The unwrapped phase $\phi_2^u=\phi^u-\phi_1^u$ then yields $\phi_2(4xx_0)$. The function $W_2(x_2^2-x_1^2)$ is reconstructed by mapping $W_2(4xx_0)$ to $W_2(x_2^2-x_1^2)$ with $x=(x_2^2-x_1^2)/4x_0$. This way the function $W(x_1,x_2)$ is reconstructed with 8-shot intensity measurement. We note that the shear size x_0 should be smaller than one-third of the difference between the diameter of the beam and the spatial coherence length, such that the overlap length of the sheared beams at the output exceeds the coherence length of the optical field, and it should be large enough for the imaging system to be able to spatially resolve it. We further note that, although for measuring a spatially non-stationary $W(x_1,x_2)$ one requires 8-shot intensity measurements, a spatially stationary function can be measured using only four intensity shots.

To test our measurement scheme, we have prepared sources that generate both non-stationary and stationary fields, as illustrated in figures 1(a)–(c). Source I figure 1(a) consist of an LED, which serves as a spatially incoherent source. The cross-spectral density of this source is given by the Van

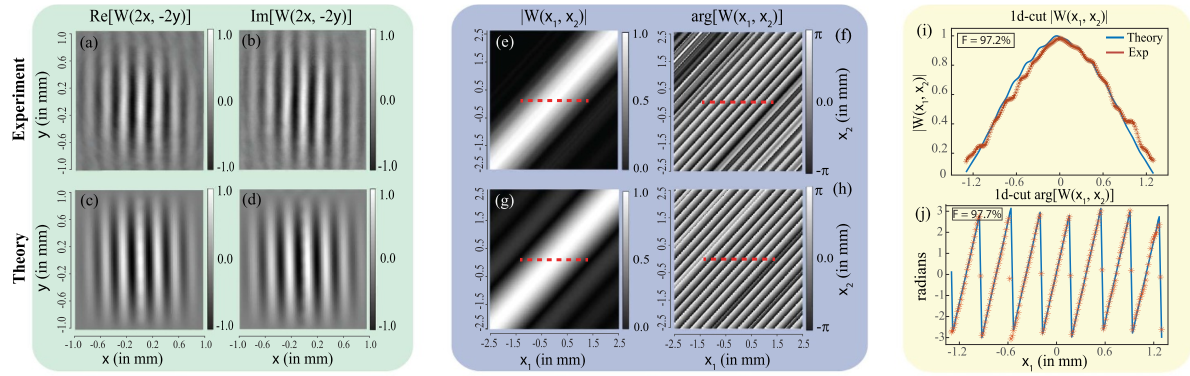

Figure 4. Source II: (a) and (b) The measured $\mathrm{Re}[W(2x,-2y)]$ and $\mathrm{Im}[W(2x,-2y)]$. (c) and (d) The theoretical $\mathrm{Re}[W(2x,-2y)]$ and $\mathrm{Im}[W(2x,-2y)]$. (e) and (f) The experimentally reconstructed $|W(x_1,x_2)|$ and $\arg[W(x_1,x_2)]$. (g) and (h) The theoretical $|W(x_1,x_2)|$ and $\arg[W(x_1,x_2)]$. (i) and (j) The 1d-cut of $|W(x_1,x_2)|$ and $\arg[W(x_1,x_2)]$ along the dotted red line.

Cittert–Zernike theorem [8], expressed as:

$$W(x_1,y_1;x_2,y_2) = \frac{\kappa e^{\iota\psi}}{(\lambda z)^2}\iint_{-\infty}^{\infty} I(x',y') \exp\left[\iota\frac{2\pi}{\lambda z}(\Delta x x' + \Delta y y')\right]\mathrm{d}x'\mathrm{d}y' \tag{11}$$

where the phase factor ψ is given by

$$\psi = \frac{\pi}{\lambda z}\left[\left(x_2^2+y_2^2\right)-\left(x_1^2+y_1^2\right)\right] \tag{12}$$

where $\mathrm{I}(x',y')$ is the intensity distribution at the source and z is the distance between the source and the observation plane. This non-stationary field is of the form $W(x_1,y_1;x_2,y_2) = W_1(x_2-x_1,y_2-y_1)W_2(x_2^2-x_1^2,y_2^2-y_1^2)$ (for details, see appendix A, section 1). Source II, III and IV are depicted in figures 1(b), (c) and 6(a) respectively consist of LEDs positioned at the back focal plane of a converging lens. The composite system of a planar spatially incoherent source with a converging lens forms the spatially partially coherent source [36]. The cross-spectral density function of this system at any propagation distance z after the lens is given by:

$$W(x_1,y_1;x_2,y_2,z) = \int_{-\infty}^{\infty} I_s(x',y')\,\mathrm{e}^{-\mathrm{i}\frac{2\pi}{\lambda f}(\Delta x x'+\Delta y y')}\mathrm{d}x'\mathrm{d}y', \tag{13}$$

where $I_s(x',y')$ is the intensity distribution at the LED plane and f is the focal length of the lens. This cross-spectral density is the Fourier transform of the LED intensity distribution, and the field is spatially stationary, $W(x_1,y_1;x_2,y_2) = W_1(x_2-x_1,y_2-y_1)$ (for details, see appendix A, section 2). Since the LED intensity distributions vary for sources II, III, and IV, the corresponding cross-spectral density functions have different structures, which are shown in figures 4–6. The LEDs in figures 1(b) and (c) are high-intensity, while the LED in figure 6(a) has very low intensity.

3. Experiment

In our experiments, we use a planar light-emitting diode (LED) unit consisting of nine separate LEDs arranged in a 3×3 square grid. Each LED has dimension 0.8 mm × 0.8 mm, with a separation of 1.9 mm (see figure 1). An interference filter (IF) centered at 632 nm having a wavelength bandwidth of 10 nm before the CCD camera ensures the field is quasi-monochromatic. The phase δ is changed using the geometric phase unit in arm-1 so that t_2-t_1 and, thereby, the degree of temporal coherence remains unaffected. To find $\delta=0$, we send a known field through the interferometer and adjust the geometric phase such that the output intensity at the camera is maximum. Once the $\delta=0$ configuration is known, we switch on the field of interest and obtain different δ values by rotating the HWP. Source I is just a single LED unit as shown in figure 1(a). As LED is a spatially incoherent source, its cross-spectral density is calculated using the van Cittert–Zernike theorem and is of the form $W(x_1,y_1;x_2,y_2) = W_1(x_2-x_1,y_2-y_1)W_2(x_2^2-x_1^2,y_2^2-y_1^2)$ [8]. Two four-shot measurements are taken, one with $x_0=0; y_0=0$ and another with shear $x_0=2.5$ mm; $y_0=0$ mm. Shear is introduced using the translations stage-1 solely along the x-axis. However, simultaneous shear along both the x and y-directions can be achieved using an xy-translation stage and thus the cross-spectral density as a function of both x and y can be measured. To calculate $A_2(4xx_0)$ as defined in equation (10), we used a threshold value equal to 0.07 times the maximum value, as the signal-to-noise ratio was observed to be poor in this region and the signal fluctuated significantly near these low values. Source II shown in figures 1(b) and source III shown in figures 1(c) consist of one off-axis LED and a group of four off-axis LEDs, respectively, kept at the back focal plane of a plano-convex lens of focal length 45 cm. Both sources are spatially stationary and have the cross spectral density function of the form $W(x_1,x_2) = W(x_2-x_1)$ and is calculated by taking the Fourier transform of the spectral density of the LED [30, 36].

The experimental results and analysis corresponding to source I, source II and source III have been presented in figures 2, 4, and 5, respectively. Figure 3 illustrates the two individual intensities and the difference intensity for the $\mathrm{Re}[W(2x,-2y)]$ in figure 2(a). It illustrates that our difference intensity protocol significantly enhances the measurement accuracy, increasing it from 80% to 95% (See appendix D for further details on the effective suppression of background

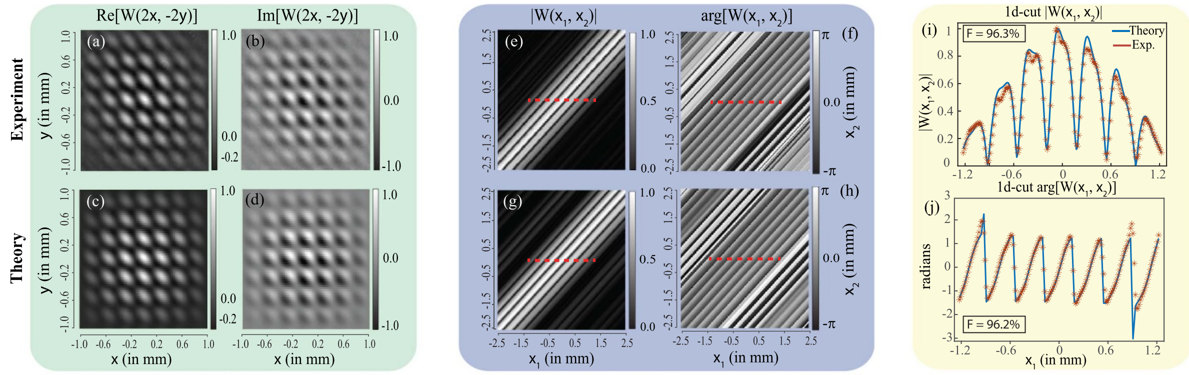

Figure 5. Source III: (a) and (b) The measured Re$[W(2x,-2y)]$ and Im$[W(2x,-2y)]$. (c) and (d) The theoretical Re$[W(2x,-2y)]$ and Im$[W(2x,-2y)]$. (e) and (f) The experimentally reconstructed $|W(x_1,x_2)|$ and arg$[W(x_1,x_2)]$. (g) and (h) The theoretical $|W(x_1,x_2)|$ and arg$[W(x_1,x_2)]$. (i) and (j) The 1d-cut of $|W(x_1,x_2)|$ and arg$[W(x_1,x_2)]$ along the dotted red line.

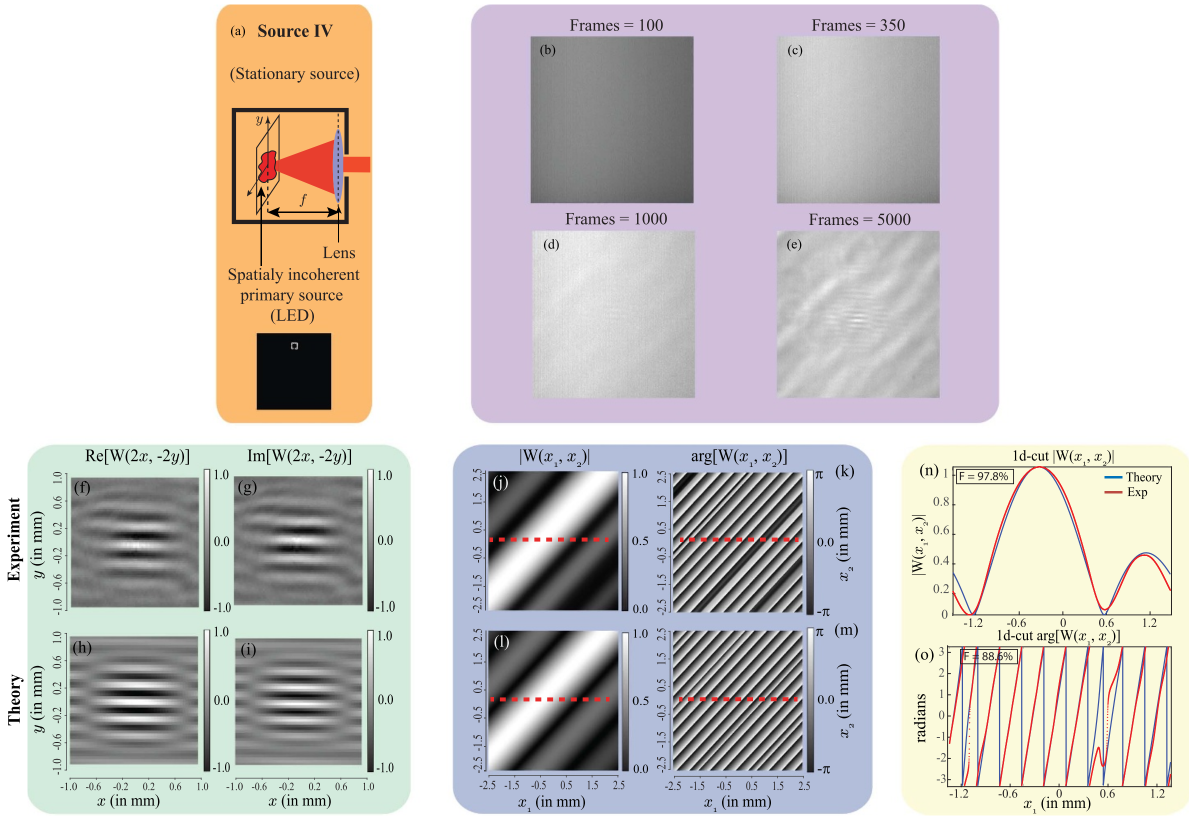

Figure 6. (a) The single-photon level source used. (b) Interferogram after accumulating 100 frames, (c) interferogram after accumulating 350 frames, (d) interferogram after accumulating 1000 frames, (e) interferogram after accumulating 5000 frames. The gain of the EMCCD camera was set at 100 for all the measurements. (f) and (g) The measured Re$[W(2x,-2y)]$ and Im$[W(2x,-2y)]$ at gain = 100 and frames accumulated = 10 000. (h) and (i) The theoretical Re$[W(2x,-2y)]$ and Im$[W(2x,-2y)]$. (j) and (k) The experimentally reconstructed $|W(x_1,x_2)|$ and arg$[W(x_1,x_2)]$. (l) and (m) The theoretical $|W(x_1,x_2)|$ and arg$[W(x_1,x_2)]$. (n) and (o) The 1d-cut of $|W(x_1,x_2)|$ and arg$[W(x_1,x_2)]$ along the dotted red line.

noise). In figures 2–5, the theory has been obtained by taking the actual image of the three LED sources and then calculating the far-field cross-spectral density function using the formulation given in [30, 36] for source I and in [8] for Source II and III (see appendix A). In figures 2–5, both theory and experimental plots for the real and imaginary parts as well as for the amplitude of the cross spectral density function have been scaled such that the maximum value of the plot is equal 1. For plotting the phase, no scaling is done. The fidelity of our experimental results, calculated using the coefficient of determination R^2 (see [37], chapter 6) and indicated in figures 2–5 are greater than 96%, showing excellent match between theory and experiment. The interferometer was operated on a standard vibration-isolated optical table, and the entire setup was enclosed in a protective box to minimize external disturbances such as air currents or acoustic noise. We note that the accurate experimental realization of δ through our geometric phase setup is very important for the accurate reconstruction of the coherence function. Nonetheless, we find that an error of θ in the geometric phase has no effect on the reconstructed amplitude of the cross-spectral density function while the reconstructed phase acquires an additional global phase of θ (see the appendix B).

In our experiment, we used a quasi-monochromatic field; however, the current method also works for broadband fields (see appendix C). This extension could broaden the method's applicability to areas such as color holography, where accurate spatial coherence measurements can help mitigate errors [38].

4. Single-photon level measurement

Source IV, shown in figure 6(a), is a spatially stationary source consisting of one off-axis LED placed at the back focal plane of a 20 cm focal length plano-convex lens. The LED has a size of 0.12 mm $\times$ 0.12 mm. An EMCCD camera was used for the measurements instead of a CCD that was employed for the first three sources. The photon flux at the EMCCD camera was calculated to be approximately 0.7 photons per frame per pixel. Figures 6(b)–(e) show the results at gain 100 after accumulating 100, 350, 1000 and 5000 frames, respectively. A faint interference pattern starts to become visible after 1000 frame accumulations. This clearly demonstrates that our system operates effectively at the single-photon level. The measurements in figures 6(f) and (g) were taken after accumulating 10 000 frames. The results, presented in figure 6, demonstrate a fidelity of 97% for amplitude and 88% for phase, indicating an excellent match between theoretical predictions and experimental data. This high degree of agreement highlights the robustness and accuracy of our method, even under low-light conditions.

5. Conclusion

In this article, we introduced and experimentally validated an interferometric method based on wavefront inversion and shearing to measure the full complex cross-spectral density function of spatially stationary and non-stationary partially coherent optical fields. The method directly retrieves the amplitude and phase profiles in eight interferogram images without requiring intensive reconstruction algorithms, significantly outperforming existing approaches [25, 26, 31, 33].

The integration of wavefront inversion interferometry with the phase-shifting technique enables the implementation of the difference intensity protocol, significantly enhancing measurement accuracy, with robustness extending to the single-photon level. This capability makes it a powerful tool for characterizing the complex cross-spectral density function of single photons generated through spontaneous parametric down-conversion (SPDC) process. As the cross-spectral density function corresponds to the density matrix elements in the quantum picture, its measurement can infer the spatial purity, an essential parameter for quantum information protocols [39–41].

This method is poised to have applications in a wide range of fields that require accurate spatial coherence characterization, including astronomical imaging to overcome the effects of atmospheric turbulence [42], microscopy for high depth-of-field imaging [43, 44], non-line-of-sight imaging to obtain information about the object's distance [9], optical encryption [10] and optical communication [45]. By providing precise measurements of the spatial coherence function, our technique is expected to significantly improve performance in each of these applications. Additionally, the method's adaptability to both high and low-light conditions further enhances its utility, making it a versatile solution for next-generation optical systems.

Data availability statement

All data that support the findings of this study are included within the article (and any supplementary files).

Acknowledgments

PM acknowledges the Prime Minister Research Fellowship (PMRF), Government of India.

Conflicts of interest

The authors declare no conflicts of interest.

Funding

Science and Engineering Research Board (Grant No. STR/2021/000 035), Department of Science & Technology, Government of India (Grant No. DST/ICPS/QuST/Theme-1/2019) and National Quantum Mission (NQM) of the Department of Science and Technology, Government of India.

Appendix A. Cross-spectral density of employed light sources

A.1. Source I

The subsequent analysis is adapted from section 5.7 of [8]. For Source I we use just a LED which can reasonably be modeled as an extended collection of independent radiators. So it can be considered as a spatially incoherent source. The Van Cittert–Zernike theorem answers how exactly the cross-spectral density propagates away from the source. For a quasi-monochromatic light, the spatial cross-spectral density function propagates according to the law,

$$W(Q_1,Q_2) = \iiiint_{\Sigma} W(P_1,P_2)\exp\left[-\iota\frac{2\pi}{\lambda}(r_2-r_1)\right] \times \frac{\chi(\theta_1)}{\lambda r_1}\frac{\chi(\theta_2)}{\lambda r_2}\mathrm{d}S_1\mathrm{d}S_2 \tag{A1}$$

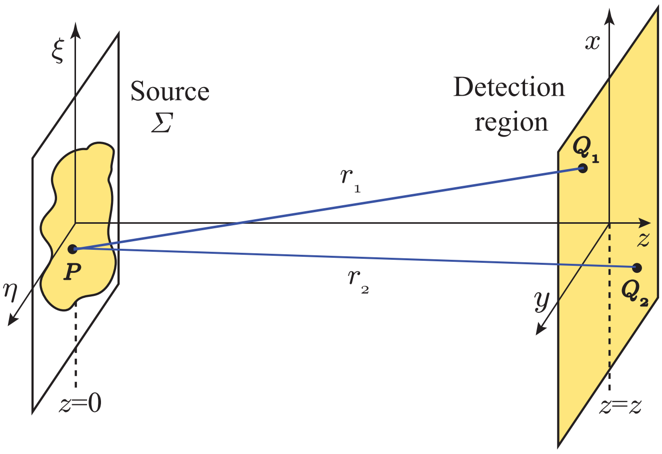

Figure A1. Geometry for derivation of Van Cittert–Zernike theorem.

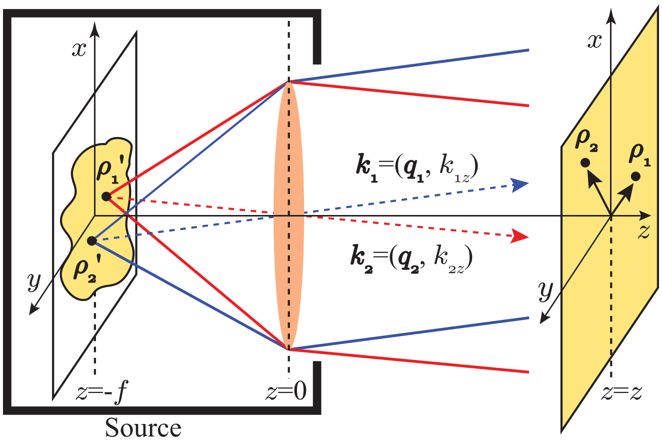

Figure A2. Schematic illustration of generation of propagation-invariant spatially-stationary field using a spatially completely-uncorrelated primary source.

where $W(Q_1,Q_2)$ and $W(P_1,P_2)$ are the cross-spectral densities at the source and detection plane respectively. $\chi(\theta)$ is the obliquity factor where θ is the angle between the line joining Q_1 and P_1 and the normal to the surface Σ at P_1.

For a spatially incoherent source, we have

$$W(P_1,P_2) = \kappa I(P_1)\,\delta(|P_1-P_2|) \tag{A2}$$

Substituting this in equation (A1) gives,

$$W(Q_1,Q_2) = \frac{\kappa}{\lambda^2}\iint_\Sigma I(P_1)\exp\left[-\iota\frac{2\pi(r_2-r_1)}{\lambda}\right] \times \frac{\chi(\theta_1)}{r_1}\frac{\chi(\theta_2)}{r_2}\mathrm{d}S \tag{A3}$$

where the geometry of the setting is illustrated in figure A1. To simplify our expression, we employ the following assumptions and approximations:

1. Far-field approximation—the dimensions of both the source and detection area are significantly smaller than the separation distance z between them,

$$\frac{1}{r_1 r_2} \approx \frac{1}{z^2} \tag{A4}$$

2. Small angle approximation,

$$\chi(\theta_1) \approx \chi(\theta_2) \approx 1. \tag{A5}$$

Following this, the cross-spectral density in the detection region takes the form

$$W(Q_1,Q_2) = \frac{\kappa}{(\lambda z)^2}\iint_\Sigma I(P_1)\exp\left[-\iota\frac{2\pi(r_2-r_1)}{\lambda}\right]\mathrm{d}S. \tag{A6}$$

In our further analysis, we make the assumption that the source and detection planes are parallel to each other, separated by a distance z. Additionally, we also employ the paraxial approximation. So,

$$r_1 = \sqrt{z^2+(x_1-x_1')^2+(y_1-y_1')^2} \approx z + \frac{(x_1-x_1')^2+(y_1-y_1')^2}{2z}$$

$$r_2 = \sqrt{z^2+(x_2-x_2')^2+(y_2-y_2')^2} \approx z + \frac{(x_2-x_2')^2+(y_2-y_2')^2}{2z}. \tag{A7}$$

Finally, we introduce the definitions $\Delta x = x_2 - x_1$ and $\Delta y = y_2 - y_1$, alongside the convention that $I(x',y')$ is zero for points (x',y') outside the finite source region Σ. This leads us to the final expression of the Van Cittert–Zernike theorem:

$$W(x_1,y_1;x_2,y_2) = \frac{\kappa e^{\iota\psi}}{(\lambda z)^2}\iint_{-\infty}^{\infty} I(x',y') \times \exp\left[\iota\frac{2\pi}{\lambda z}(\Delta x x' + \Delta y y')\right]\mathrm{d}x'\mathrm{d}y' \tag{A8}$$

where the phase factor ψ is given by

$$\psi = \frac{\pi}{\lambda z}\left[(x_2^2+y_2^2)-(x_1^2+y_1^2)\right] \tag{A9}$$

From equations (A8) and (A9) it is clear that the cross-spectral density of LED source is of the form $W(x_1,y_1;x_2,y_2) = W_1(x_2-x_1,y_2-y_1)W_2(x_2^2-x_1^2,y_2^2-y_1^2)$.

A.2. Source II, III & IV

The discussion that follows is sourced from [36]. For Sources II and III, a monochromatic, planar, spatially completely incoherent primary source is positioned at the back focal plane, $z=-f$, of a lens located at $z=0$ as depicted in figure A2. Our spatially partially coherent field source consists of this composite system of the planar primary source and the lens. The field emanating from a spatial location $\boldsymbol{\rho}'$ at a distance z is denoted as $V_s(\boldsymbol{\rho}',z)$. Given the complete spatial incoherence of our primary source, the fields $V_s(\boldsymbol{\rho}_1',-f)$ and $V_s(\boldsymbol{\rho}_2',-f)$ emerging from $\boldsymbol{\rho}_1'$ and $\boldsymbol{\rho}_2'$ at $z=-f$, respectively, are entirely uncorrelated. This lack of correlation is expressed as,

$$\langle V_s^*(\boldsymbol{\rho}_1',-f)\,V_s(\boldsymbol{\rho}_2',-f)\rangle_e = I_s(\boldsymbol{\rho}_1',-f)\,\delta(\boldsymbol{\rho}_1'-\boldsymbol{\rho}_2'). \tag{A10}$$

Here $I_s(\boldsymbol{\rho}_1',-f)$ is the intensity of the primary source at $z=-f$. In our experiments, we use LEDs as our primary incoherent sources. Here, $I_s(\boldsymbol{\rho}_1', -f)$ denotes the intensity of the primary source at $z = -f$. LED serve as our primary incoherent source as their positional correlations are modeled by the form outlined in equation (A10) [46, 47].

For our primary source characterized by equation (A10), each point on the source behaves as an independent point source. As each of these points is positioned at the back focal plane of a converging lens, the field $V_s(\boldsymbol{\rho}_1', -f)$ originating from $\boldsymbol{\rho}_1'$ undergoes transformation into a plane wave with amplitude $a(\boldsymbol{q_1})$, where $\boldsymbol{q_1}$ denotes the transverse wave-vector associated with the plane wave [48, 49]. The lens effectively converts the non-correlation of the planar source in the position basis into non-correlation in the transverse wave-vector basis. The correlations between distinct transverse wave-vectors are quantified through the angular correlation function $\mathcal{A}(\boldsymbol{q_1}, \boldsymbol{q_2})$, defined as $\mathcal{A}(\boldsymbol{q_1}, \boldsymbol{q_2}) \equiv \langle a^*(\boldsymbol{q_1}) a(\boldsymbol{q_2})\rangle_e$, where $\langle \cdots \rangle_e$ denotes the ensemble average. The angular correlation function for such a partially coherent source corresponds to the angular correlation function $\mathcal{A}(\boldsymbol{q_1}, \boldsymbol{q_2})$ at the exit face of the lens, i.e. at $z = 0$, and is expressed as,

$$\mathcal{A}(\boldsymbol{q_1}, \boldsymbol{q_2}) \equiv \langle a^*(\boldsymbol{q_1})\, a(\boldsymbol{q_2})\rangle_e = I_s(\boldsymbol{q_1})\, \delta(\boldsymbol{q_1} - \boldsymbol{q_2}). \tag{A11}$$

Here, $I_s(\boldsymbol{q_1})$ represents the spectral density of the field, exhibiting the same functional form as the source intensity. As demonstrated below, this specific form of the angular correlation function is a prerequisite for the spatially-stationary and propagation-invariant characteristics of the partially-coherent field emerging from a source.

We proceed to derive the cross-spectral density function at $z = z$ generated by such a source. As detailed in section 5.6 of [14], assuming the plane-wave amplitude at $z = 0$ is $a(\boldsymbol{q_1})$, the field $V(\boldsymbol{\rho}_1, z)$ at $z = z$ within the paraxial approximation is given by,

$$V(\boldsymbol{\rho}_1, z) = \mathrm{e}^{\mathrm{i}k_0 z} \iint_{-\infty}^{\infty} a(\boldsymbol{q_1})\, \mathrm{e}^{\mathrm{i}\boldsymbol{q_1}\cdot\boldsymbol{\rho}_1} \mathrm{e}^{-\mathrm{i}\frac{q_1^2 z}{2k_0}} \mathrm{d}\boldsymbol{q_1}. \tag{A12}$$

Here, $\boldsymbol{r_1} \equiv (\boldsymbol{\rho_1}, z)$, $\boldsymbol{k_1} \equiv (\boldsymbol{q_1}, k_{1z})$, and $k_{1z} \approx k_1 - q_1^2/(2k_1)$ with $q_1 = |\boldsymbol{q_1}|$ and $k_1 = |\boldsymbol{k_1}| = k_0 = \omega_0/c$, where ω_0 is the frequency of the field. So the cross-spectral density function $W(\boldsymbol{\rho}_1, \boldsymbol{\rho}_2, z) \equiv \langle V^*(\boldsymbol{\rho}_1, z) V(\boldsymbol{\rho}_2, z)\rangle_e$ at $z = z$ is

$$W(\boldsymbol{\rho}_1, \boldsymbol{\rho}_2, z) = \iint_{-\infty}^{\infty} \mathcal{A}(\boldsymbol{q_1}, \boldsymbol{q_2}) \times \mathrm{e}^{-\mathrm{i}\boldsymbol{q_1}\cdot\boldsymbol{\rho}_1 + \mathrm{i}\boldsymbol{q_2}\cdot\boldsymbol{\rho}_2} \mathrm{e}^{-\mathrm{i}\frac{(q_1^2 - q_2^2)z}{2k_0}} \mathrm{d}\boldsymbol{q_1}\mathrm{d}\boldsymbol{q_2}. \tag{A13}$$

Equation (A13) dictates the evolution of spatial correlations in the field, as denoted by the cross-spectral density function, during propagation in the region $z > 0$ after passing through the lens. Substituting the expression for the angular correlation function from equation (A11) into equation (A13), we acquire,

$$W(\boldsymbol{\rho}_1, \boldsymbol{\rho}_2, z) = W(\boldsymbol{\Delta}\rho, z) = \int_{-\infty}^{\infty} I_s(\boldsymbol{q})\, \mathrm{e}^{-\mathrm{i}\boldsymbol{q}\cdot\boldsymbol{\Delta}\rho} \mathrm{d}\boldsymbol{q}, \tag{A14}$$

where $\boldsymbol{\Delta}\rho = \boldsymbol{\rho_1} - \boldsymbol{\rho_2}$. We see that the cross-spectral density function $W(\boldsymbol{\Delta}\rho, z)$ in equation (A14) follows coherent mode representation, where the coherent modes correspond to plane waves. The generated field exhibits the following characteristics: (1) *Propagation invariance*—the cross-spectral density function and intensity remain constant regardless of changes in z. (2) *Spatial stationarity at a given* z, at least in a broad sense—this is evident from the fact that the intensity $I(\boldsymbol{\rho}, z)$ does not depend on $\boldsymbol{\rho}$, while the cross-spectral density function depends only on $\Delta\boldsymbol{\rho}$. (3) *The cross-spectral density function* $W(\boldsymbol{\Delta}\rho, z)$ *of the field is the Fourier transform of its spectral density* $I_s(\boldsymbol{q})$. Furthermore, as the spectral density mirrors the intensity pattern of the primary source, the cross-spectral density function of the field seamlessly transforms into the Fourier representation of the primary source's intensity profile. It's noteworthy that this methodology liberates the intensity function $I_s(\boldsymbol{q_1})$ of the primary incoherent source from constraints—whether continuous, of finite dimensions, or structured as an ensemble of discrete points.

Appendix B. Error analysis for geometric phase

From equation (3) in the main text we see that the difference in the intensities of the two interferograms is,

$$\begin{aligned}\Delta I_{\mathrm{out}}(x,y) &= I_{\mathrm{out}}^{\delta_c}(x,y) - I_{\mathrm{out}}^{\delta_d}(x,y)\\ &= 2k_1k_2\{\mathrm{Re}\,[\mathrm{W}(-x+x_0, y; x+x_0, -y)]\\ &\quad\times(\cos(\delta_c) - \cos(\delta_d))\\ &\quad - \mathrm{Im}\,[\mathrm{W}(-x+x_0, y; x+x_0, -y)]\\ &\quad\times(\sin(\delta_c) - \sin(\delta_d))\}.\end{aligned} \tag{A15}$$

The geometric phase setup, depicted in arm 1 of figure 1(d) in the main text, involves two quarter-waveplates (QWP1) oriented at 45° with respect to the polarization of light, with a half-waveplate (HWP) placed in between. Rotating the HWP by an angle ϕ with respect to the polarization direction of the incoming linearly polarized light introduces a relative phase difference of 2ϕ between the two arms, denoted as $\delta = 2\phi$. We obtain measurements at different δ values by rotating the HWP. The precision of rotation relies on the accuracy of the HWP rotation. In our setup, the HWP was affixed to an automated rotation stage, ensuring uniform error across all measurements. Let θ be the error in setting the phase difference between the two arms, $\delta_{c,d}$. Then,

$$\begin{aligned}\Delta I_{\mathrm{out}}(x,y) = 2k_1k_2\,[&W_{\mathrm{R}}\{\cos\delta_c\cos\theta - \sin\delta_c\sin\theta\\ &-\cos\delta_d\cos\theta + \sin\delta_d\sin\theta\}\\ &- W_{\mathrm{Im}}\{\sin\delta_c\cos\theta + \cos\delta_c\sin\theta - \sin\delta_d\cos\theta\\ &-\cos\delta_d\sin\theta\}].\end{aligned} \tag{A16}$$

where $W_{\mathrm{R}} = \mathrm{Re}[W(-x+x_0, y; x+x_0, -y)]$ and $W_{\mathrm{Im}} = \mathrm{Im}[W(-x+x_0, y; x+x_0, -y)]$. From here onwards we adopt this renaming for brevity.

Putting $\delta_c = 0$ and $\delta_d = \pi$ we get,

$$\Delta I_{\mathrm{out}}(x,y)|_1 = 4k_1k_2\{(\cos\theta)\, W_{\mathrm{R}} - (\sin\theta)\, W_{\mathrm{Im}}\}. \tag{A17}$$

Putting $\delta_c = 3\pi/2$ and $\delta_d = \pi/2$ we get,

$$\Delta I_{\text{out}}(x,y)|_2 = 4k_1k_2\{(\sin\theta)W_{\text{R}} + (\cos\theta)W_{\text{Im}}\}. \tag{A18}$$

Squaring and adding equations (A17) and (A18) we get,

$$\begin{aligned}\Delta I^2_{\text{out}}(x,y)|_1 + \Delta I^2_{out}(x,y)|_2 &= (4k_1k_2)^2\left(W^2_{\text{R}} + W^2_{\text{Im}}\right)\\ &= 16k_1^2k_2^2|W|^2\end{aligned} \tag{A19}$$

where $|W|$ is the amplitude of the cross-spectral density function. So we can write,

$$|W| = \frac{\sqrt{\Delta I^2_{\text{out}}(x,y)|_1 + \Delta I^2_{out}(x,y)|_2}}{4k_1k_2}. \tag{A20}$$

We see that amplitude of the cross-spectral density function is unaffected by the error in δ.

From equations (A17) and (A18) we see that the phase profile of the cross-spectral function is given by,

$$\arg[\text{W}] = \tan^{-1}\left[\frac{\Delta I_{\text{out}}(\boldsymbol{\rho})|_2}{\Delta I_{\text{out}}(\boldsymbol{\rho})|_1}\right] = \tan^{-1}\left[\frac{W_{\text{Im}} + (\tan\theta)W_{\text{R}}}{W_{\text{R}} - (\tan\theta)W_{\text{Im}}}\right]. \tag{A21}$$

Therefore the error in the phase profile of the cross-spectral density function is,

$$\begin{aligned}\text{Error}(\arg[\text{W}]) = \tan^{-1}&\left[\frac{W_{\text{Im}} + (\tan\theta)W_{\text{R}}}{W_{\text{R}} - (\tan\theta)W_{\text{Im}}}\right]\\ &- \tan^{-1}\left[\frac{W_{\text{Im}}}{W_{\text{R}}}\right] = \theta.\end{aligned} \tag{A22}$$

We find that an error of θ in the geometric phase has no effect on the reconstructed amplitude of the cross-spectral density function while the error in the reconstructed phase increases only linearly with θ.

Another way to interpret the linear phase deviation described in equation (A22) is to view it as a constant global phase offset. As seen from equations (A17) and (A18), the measured cross-spectral density function takes the form,

$$W_{\text{measured}} = W_{\text{incoming}}\mathrm{e}^{i\theta} \tag{A23}$$

where θ is a spatially constant phase shift that arises if the HWP is not initially aligned with the polarization of the input light. This global phase offset corresponds precisely to the linear phase deviation introduced in equation (A22). Since it is uniform across space, it does not affect spatial coherence structure and can be eliminated by proper alignment.

Appendix C. Space-time correlation

Section 2 detailed the space-frequency correlation, which is used to measure the spatial coherence of a monochromatic field. In this section, we demonstrate how our proposed technique extends to the measurement of space-time correlation, thereby broadening the spatial coherence analysis to broadband fields.

The field from the source enters the interferometer and reaches the camera after travelling for times t_1 and t_2 through the two arms of the interferometer. The electric field at V(x,y;t) at the camera plane at time t is given by

$$\begin{aligned}V(x,y;t) &= k_1V(x_1,y_1;t-t_1) + k_2V(x_2,y_2;t-t_2)\\ &= k_1\int_{-\infty}^{\infty}E(x_1,y_1;\omega)\,\mathrm{e}^{-\mathrm{i}\omega(t-t_1)}\mathrm{d}\omega\\ &\quad + k_2\int_{-\infty}^{\infty}E(x_2,y_2;\omega)\,\mathrm{e}^{-\mathrm{i}\omega(t-t_2)}\mathrm{d}\omega\end{aligned} \tag{A24}$$

where $V(x_1,y_1;t-t_1)$ and $V(x_2,y_2;t-t_2)$ are the electric field vibrations at the source points (x_1,y_1) and (x_2,y_2) at time $t-t_1$ and $t-t_2$ respectively. We consider the optical field to be temporally stationary, meaning that its frequency components are uncorrelated,

$$\begin{aligned}&\langle E^*(x_1,y_1;\omega_1)\,E(x_2,y_2;\omega_2)\rangle_e\\ &\quad = W(x_1,y_1;x_2,y_2;\omega_1)\,\delta(\omega_1-\omega_2)\end{aligned} \tag{A25}$$

where $W(x_1,y_1;x_2,y_2;\omega)$ is the cross-spectral density function. The intensity at the detector can now be written as,

$$\begin{aligned}I_{\text{out}}(x,y;t) = &\ |k_1|^2I_1(x_1,y_1;t-t_1) + |k_2|^2I_2(x_2,y_2;t-t_2)\\ &+ 2k_1k_2\text{Re}[\Gamma(x_1,y_1;x_2,y_2;\tau)]\cos\delta\\ &- 2k_1k_2\text{Im}[\Gamma(x_1,y_1;x_2,y_2;\tau)]\sin\delta,\end{aligned} \tag{A26}$$

where $\tau = t_2 - t_1$, $\delta = \beta_2 - \beta_1$, $I_i(x_i,y_i;t-t_i) = \int_{-\infty}^{\infty}|E_{\text{in}}(x_i,y_i;\omega)|^2\mathrm{e}^{-\mathrm{i}\omega(t-t_i)}\mathrm{d}\omega$ for $i = 1,2$ are the intensities from the two arms and $\Gamma(x_1,y_1;x_2,y_2;\tau) = \int_{-\infty}^{\infty}W(x_1,y_1;x_2,y_2;\omega)\mathrm{e}^{-\mathrm{i}\omega\tau}\mathrm{d}\omega$ is the cross-correlation function which is the Fourier transform of the cross-spectral density function.

For a temporally stationary field, the cross-correlation function depends only on the time difference τ, which corresponds to the path difference, Δz, between the two arms. Therefore, for a broadband field, the temporal correlations also come into the picture. The spatial coherence of a broadband field is obtained when $\tau = 0$ (i.e. $\Delta z = 0$), which can be achieved by adjusting the translation stage in arm 2 of the interferometer. As described in section 2, we control the phase between the arms of the interferometer using waveplates, and the real and imaginary parts of the cross-correlation function are measured via the intensity difference method. So, our method, in principle, can be used for measuring the spatial coherence of broadband fields.

In practice, translation stages have finite precision, introducing errors in the measurement. The temporal coherence length is inversely proportional to the field's spectral width, meaning a larger spectral width requires greater measurement precision. The absolute error depends upon the functional form of the cross-correlation function. In our setup, we use a translation stage with $\Delta z = 0.5\,\mu$m, yielding $\tau = 1.67\times10^{-15}$ s. For a multi-wavelength regime where the field is quasi-monochromatic around multiple central wavelengths, precise spatial coherence measurements can be achieved using a colored CCD camera, even with a finite-precision translation stage. In this case, each frequency component would experience a different phase difference between the two interferometric arms because of the term $\omega\tau$ in the phase factor δ in equation (2) of the manuscript. To accurately measure the real and imaginary components of the cross-spectral density function for each wavelength, the orientation of the HWP (inducing the geometric phase) would need to be adjusted individually for each wavelength.

Appendix D. Noise measurement

To quantitatively validate the noise-insensitive nature of our protocol, we conducted a background noise analysis by recording intensity maps with the light source turned off. Measurements were performed at four phase shifts ($\delta = 0, \pi, \pi/2, 3\pi/2$), each averaged over 100 frames, to isolate phase-insensitive background noise from any signal contributions.

The intensity values before subtraction were as follows: at $\delta = 0$, the mean was 526.6747, the standard deviation was 9.0512, and the maximum value was 547.3400; at $\delta = \pi$, the mean was 526.4349, the standard deviation was 9.0498, and the maximum value was 546.5900; at $\delta = \pi/2$, the mean was 526.3869, the standard deviation was 9.0547, and the maximum value was 547.0800; and at $\delta = 3\pi/2$, the mean was 525.9892, the standard deviation was 9.0399, and the maximum value was 545.9700.

After applying the difference-intensity protocol, the residual maps showed significant suppression of the background signal. For the real part (from the difference between $\delta = 0$ and π), the mean was 2.7730, the standard deviation was 2.0961, and the maximum value was 17.4100. For the imaginary part (from the difference between $\delta = \pi/2$ and $3\pi/2$), the mean was 2.7893, the standard deviation was 2.1077, and the maximum value was 20.6200.

These results demonstrate that the protocol effectively cancels phase-insensitive background noise, reducing both the average background level and its fluctuations under realistic experimental conditions.

ORCID iDs

Pranay Mohta 0009-0009-7847-8956
Abhinandan Bhattacharjee 0000-0002-0646-2404

References

[1] Dhalla A-H, Migacz J V and Izatt J A 2010 *Opt. Lett.* **35** 2305
[2] Redding B, Choma M A and Cao H 2012 *Nat. Photon.* **6** 355–9
[3] Redding B, Cerjan A, Huang X, Lee M L, Stone A D, Choma M A and Cao H 2015 *Proc. Natl Acad. Sci.* **112** 1304–9
[4] Naik D N, Ezawa T, Miyamoto Y and Takeda M 2009 *Opt. Express* **17** 10633
[5] Naik D N, Singh R K, Ezawa T, Miyamoto Y and Takeda M 2011 *Opt. Express* **19** 1408
[6] Ricklin J C and Davidson F M 2002 *J. Opt. Soc. Am. A* **19** 1794
[7] Dong Y, Wang F, Zhao C and Cai Y 2012 *Phys. Rev. A* **86** 013840
[8] Goodman J W 2015 *Statistical Optics* (Wiley)
[9] Batarseh M, Sukhov S, Shen Z, Gemar H, Rezvani R and Dogariu A 2018 *Nat. Commun.* **9** 3629
[10] Peng D, Huang Z, Liu Y, Chen Y, Wang F, Ponomarenko S A and Cai Y 2021 *PhotoniX* **2** 6
[11] Liu X and Zhao D 2015 *Opt. Commun.* **354** 250–5
[12] Lajunen H and Saastamoinen T 2011 *Opt. Lett.* **36** 4104
[13] Xu Y, Guan Y, Liu Y, Lin S, Zhu X, Cai Y, Yu J and Gbur G 2023 *Opt. Lett.* **48** 2631
[14] Mandel L and Wolf E 1995 *Optical Coherence and Quantum Optics* (Cambridge University Press)
[15] Turunen J, Vasara A and Friberg A T 1991 *J. Opt. Soc. Am. A* **8** 282
[16] Santarsiero M and Borghi R 2006 *Opt. Lett.* **31** 861
[17] Efimov A 2013 *Opt. Lett.* **38** 4522
[18] Rezvani Naraghi R, Gemar H, Batarseh M, Beckus A, Atia G, Sukhov S and Dogariu A 2017 *Opt. Lett.* **42** 4929
[19] Nugent K A 1992 *Phys. Rev. Lett.* **68** 2261–4
[20] Wood J K, Sharma K A, Cho S, Brown T G and Alonso M A 2014 *Opt. Lett.* **39** 4927
[21] Koivurova M, Partanen H, Turunen J and Friberg A T 2017 *Appl. Opt.* **56** 5216
[22] Mejía Y and González A I 2007 *Opt. Commun.* **273** 428–34
[23] Hooshmand-Ziafi H, Dashtdar M and Hassani K 2020 *Opt. Lett.* **45** 3737
[24] Anderson B L 1993 *Opt. Eng., Bellingham* **32** 926
[25] Rydberg C and Bengtsson J 2007 *Opt. Express* **15** 13613
[26] Petruccelli J C, Tian L and Barbastathis G 2013 *Opt. Express* **21** 14430
[27] Huang Z, Chen Y, Wang F, Ponomarenko S A and Cai Y 2020 *Phys. Rev. Appl.* **13** 044042
[28] Wessely H W and Bolstad J O 1970 *J. Opt. Soc. Am.* **60** 678
[29] Breckinridge J B 1972 *Appl. Opt.* **11** 2996
[30] Bhattacharjee A, Aarav S and Jha A K 2018 *Appl. Phys. Lett.* **113** 051102
[31] Halder A, Partanen H, Leinonen A, Koivurova M, Hakala T K, Setälä T, Turunen J and Friberg A T 2020 *Opt. Lett.* **45** 4260
[32] Takeda M, Ina H and Kobayashi S 1982 *J. Opt. Soc. Am.* **72** 156
[33] Torcal-Milla F J, Lobera J, Roche E M, Lopez A M, Palero V, Andres N and Arroyo M P 2023 *Opt. Lett.* **48** 3127
[34] Karan S, Ruchi, Mohta P and Jha A K 2022 *Appl. Opt.* **61** 8302
[35] Jha A K, Malik M and Boyd R W 2008 *Phys. Rev. Lett.* **101** 180405
[36] Aarav S, Bhattacharjee A, Wanare H and Jha A K 2017 *Phys. Rev. A* **96** 033815
[37] Glantz S A, Slinker B K and Neilands T B 2001 *Primer of Applied Regression & Analysis of Variance* vol 654 (McGraw-Hill, Inc.)
[38] Yan H, Sun Y, Lin Y, Chu F and Wan W 2023 *Opt. Express* **31** 22649
[39] Scarani V, Bechmann-Pasquinucci H, Cerf N J, Dušek M, Lütkenhaus N and Peev M 2009 *Rev. Mod. Phys.* **81** 1301–50
[40] Girolami D 2014 *Phys. Rev. Lett.* **113** 170401
[41] Patoary A S M, Kulkarni G and Jha A K 2019 *J. Opt. Soc. Am. B* **36** 2765
[42] Roddier F 1988 *Phys. Rep.* **170** 97–166

[43] Potuluri P, Fetterman M and Brady D 2001 *Opt. Express* **8** 624
[44] Weigel D, Babovsky H, Kiessling A and Kowarschik R 2015 *Opt. Commun.* **342** 102–8
[45] Liu Y, Zhang X, Dong Z, Peng D, Chen Y, Wang F and Cai Y 2022 *Phys. Rev. Appl.* **17** 024043S
[46] Tziraki M, Jones R, French P, Melloch M and Nolte D 2000 *Appl. Phys. B* **70** 151–4
[47] Di Lorenzo Pires H, Woudenberg J and van Exter M P 2010 *Opt. Lett.* **35** 889
[48] Born M and Wolf E 2013 *Principles of Optics: Electromagnetic Theory of Propagation, Interference and Diffraction of Light* (Elsevier)
[49] Goodman J W 2005 *Introduction to Fourier Optics* (Roberts and Company Publishers)